The importance of smoothness constraints on spectral object reflectances when modeling metamer mismatching

Tarek Stiebel and Dorit Merhof
Institute of Imaging & Computer Vision - RWTH Aachen University
Kopernikusstraße 16, 52074 Aachen
Tarek.stiebel@lfb.rwth-aachen.de

Abstract

This paper analyzes the influence of multi-spectral imaging onto the severity of metamer mismatching, in particular in the context of color-accuracy of machine vision. Camera signals associated with simulated as well as real world multi-spectral imaging systems when viewing different objects under different lighting conditions were calculated. Based on the calculated camera signals, the associated MMBs were computed when changing towards the CIE standard observer under illuminant D65.
The results show that an increased number of channels used in multi-spectral imaging systems do not necessarily decrease the severity of metamer mismatching. However, it is also shown that this is due to the limited capabilities of current image acquisition models which are not able to correctly compute a realistic MMB as they neglect any smoothness constraints on spectral object reflectances.

1. Introduction

Whenever the accurate measurement of color is desired, common RGB-cameras usually do not suffice. This is due to metamerism, a phenomenon originally introduced in the context of human color vision. Excluding optimal colors, a tristimulus can be associated with a set of metameric lights, i.e. lights inducing an identical tristimulus value with respect to the human observer. However, such a set of metameric lights does not have to remain metameric when the observer changes. Instead, the originally metameric set of lights may induce a non-singleton set of tristimuli, the so-called metamer mismatch volume/body (MMB) [12, 4, 23]. The effect itself is known as metamer mismatching [24] and it always occurs if the Luther-Ives condition [9, 14] is broken, i.e. there is no linear dependency between the respective color-matching functions. This is analogously the case, when transforming from machine color vision to human color vision.

A spectral stimulus can typically be divided into two parts, an illuminant and a spectral object reflectance. The set of all objects inducing an identical tristimulus for a specific observer under a certain illuminant is said to be metameric with respect to the observer under the current illuminant. While a metameric set of spectral object reflectances with respect to a combination of an observer and an illuminant will lead to identical tristimuli when viewed by this particular combination, the set might differ in appearance, when viewed by another combination. The set does not necessarily have to remain metameric when the observer, the illuminant or both are changed, leading to metamer mismatching [12, 24].
The concept of metamerism may be abstracted to cameras, which is sometimes explicitly denoted as device metamerism. Different lights entering the camera system may lead to identical camera-signals. A possible way to reduce device metamerism is by employing multi-spectral imaging with the supreme goal being spectral reconstruction of viewed objects based on observed camera signals. Achieving this goal would allow to virtually illuminate images to ones own desire or create tailor-made colorimetric information for individual observers. Examples of reconstruction methods are the PCA [11, 15, 22], Pseudoinverse [18], the kernel approach (including the Wiener estimation) [8, 21], the matrix R method [28], or, following the current trend of machine learning, neural networks [16]. However, spectral reconstruction is usually an unsolvable problem due to metamerism. Given an observed camera signal, there is no unambiguous assignment of reflectance functions to represent a viewed object.
This work contends itself to the task of color management, i.e. the conversion of an observed camera signal towards a device independent representation. There exist numerous algorithms and variations tackling this challenge. All of them can be separated into two groups, namely target-based and model-based. Where the first group tries to learn a unique relationship based on known correspondences of camera signals and color coordinates, e.g. from raw-RGB

to sRGB, model based approaches consider the image acquisition process and pay tribute to the fact, that there is no unique relationship. Examples of target-based approaches are a linear transformation [17], polynomial modeling [7] or neural networks [26]. The most advanced model-based algorithms are capable of calculating the theoretical MMB, e.g. the algorithm proposed by Logvinenko [12] or the algorithm proposed by Centore [5]. However, they are restricted to three dimensional color vision and are too slow, when the evaluation of larger data sets is desired.

This work makes use of a novel algorithm [23], allowing to compute the theoretical MMBs even when using multi-spectral imaging. The goal of this work is to evaluate and quantify the achievable color accuracy of multi-spectral imaging systems in terms of the theoretical MMB. The focus is the analysis of device metamerism, in particular the relationship between multi-spectral imaging systems and the resulting MMBs, when converting a seen camera signal towards the CIE standard observer under the illuminant D65. While it is certainly expected that the degree of metamer mismatching decreases as the amount of camera channels increases, it will be shown that this is not necessarily the case from a theoretical point of view.

2. Computation

For the sake of clarity, necessary terminology will be introduced first. Both human observers and camera systems will in the following be referred to as a *sensing device*. Likewise, the term metamerism is not to be seen as restricted to human color vision but on an abstract level also comprising device metamerism. The combination of a sensing device with an illuminant will be referred to as a *color mechanism* [13]. A color mechanism is directly associated with its *spectral weighting functions*, consisting of the spectral sensitivity functions of the sensing device and the *spectral power distribution* (SPD) of the illuminant. A viewed object, given by its spectral reflectance, will induce a *color signal* when viewed by a color mechanism.
At all times, the considered wavelengths range from λ_{min} =380nm to λ_{min} =780nm in 1nm steps. Color signals were calculated using the common model

$$\varphi_i(r) = \int_{\lambda_{min}}^{\lambda_{max}} \sigma_i(\lambda) r(\lambda) d\lambda \quad (i = 1, ..., n), \qquad (1)$$

where $\Phi = (\varphi_1, ..., \varphi_n)^T$ denotes the color signal an object with the spectral reflectance function $r(\lambda)$ induces when viewed by the n-dimensional color mechanism associated with the spectral weighting functions $\sigma_i(\lambda)$.
Given a computed color signal, the MMB associated with a change of color mechanism towards the CIE standard observer under illuminant D65 was computed using the algorithm proposed by Stiebel et al. [23]. This is an extended version of the algorithm proposed by Logvinenko et al. [12], making it applicable to multi-spectral imaging as well as improving the computational time. It allows to calculate the precise theoretical boundary surface of the MMB by modeling the creation of a color signal with Equation 1 and based on the assumption that spectral object reflectances may neither be negative nor exceed the value 1, i.e. $r(\lambda) \in [0, 1] \; \forall \; \lambda$.
An important, yet frequently neglected, aspect of computing the theoretical MMB is the fact, that it is only possible to compute individual points on the boundary enclosing the MMB [4, 12, 23]. Thus, only a sampling of the boundary surface can be achieved. A natural question to ask is how to perform this sampling in the most precise as well as efficient way. It has been established that, with the MMB being a closed convex set, its boundary surface can be expressed using spherical coordinates with the origin being in a central position inside the MMB [12, 23]. In this work, the boundary surface was sampled using an icosahedral geodesic grid, which can be seen as a set of uniformly distributed points upon a spherical surface. It is based upon the successive subdivision of the faces of an icosahedron. The amount of resulting points, and therefore the sampling density of the surface, is controlled by the amount of successively performed subdivisions, also called tessellation order. Figure 1 illustrates the approach.

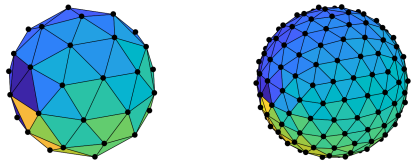

(a) Tesselation order 1 (b) Tesselation order 2

Figure 1: Visualization of the employed sampling technique based on a zonohedral geodesic grid.

2.1. Experimental Setup

The following information is needed in order to calculate the MMB associated with a change of color mechanism: the spectral sensitivity functions of the respective sensing devices, the respective illuminants given by their SPD, and, finally, the color signal as observed by one of the color mechanisms.
Since the conversion towards the CIE standard observer under illuminant D65 has been investigated in this work, one color mechanism remained always the same. Regarding

the other color mechanism, the illuminants considered are the CIE standard illuminants E, D50, D65, D99, A, C, F4, F8, F11, covering a wide range of possible light sources. The set of camera systems is twofold. The first subset is based upon simulated multi-spectral imaging systems, with individual channels being modeled using Gaussian functions [23]. The second subset consists of real multi-spectral imaging systems, which have been characterized by measuring their spectral sensitivity.

The same simulated multi-spectral imaging systems as in [23] have been used. This means that the individual spectral sensitivity functions were modeled using Gaussian functions

$$s_i(\lambda) = e^{\frac{\lambda-\lambda_{ci}}{2\sigma^2}}, \tag{2}$$

where λ_{ci} denotes the central position of the i'th channel. The width of the curve is controlled by the standard deviation σ. Given a channel count of n, the central positions of all Gaussians were positioned in equidistant intervals between 400nm and 700nm. In total, channel counts from 3 to 9 were considered. For a better understanding, Figure 2a displays the simulated spectral sensitivities in case of a 6-channel system.

Initially, the standard deviation was chosen such that neighboring channels intersect at one times their variance, i.e. $\sigma = \sigma_n = \frac{700nm-400nm}{n}$. However, in order to test the influence of the filter width onto metamer mismatching, different values for the standard deviation were considered as well.

For comparison, a total of three real cameras have been analyzed. A RGB-camera is represented by a Basler AvA2300-25gc. The first multi-spectral system is a 6-channel system, realized as a stereo setup combining two of the mentioned RGB-cameras respectively extended with interference filters to achieve wavelength multiplexing. Last, there is a 7-channel multi-spectral camera consisting of a monochrome camera and a filter wheel.

The spectral sensitivity functions of each camera system were individually measured using a monochromator setup. A narrow band light stimulus, created by the monochromator, is viewed in parallel by both the camera to be measured as well as a spectrophotometer. Based on an entire set of created light stimuli in the wavelength range from 380nm to 780 in 1nm steps, the algorithm proposed by Paulus [19] was used to calculate the spectral sensitivity functions. The resulting sensitivity functions are shown in Figure 2.

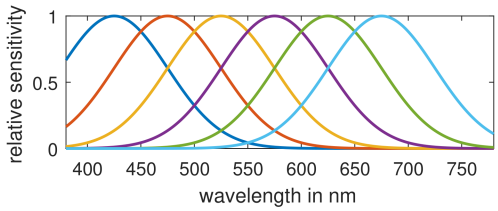

(a) Simulated 6D imaging device with $\sigma = \sigma_6$

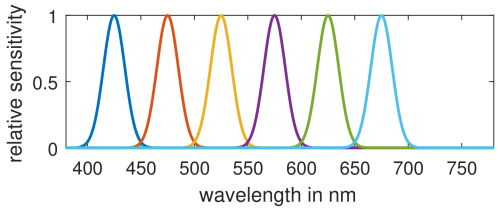

(b) Simulated 6D imaging device with $\sigma = 0.2\sigma_6$

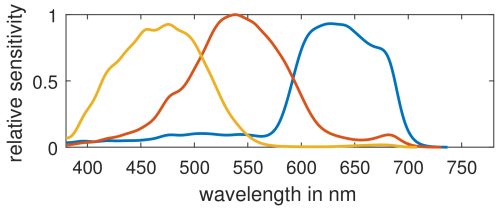

(c) RGB-Camera

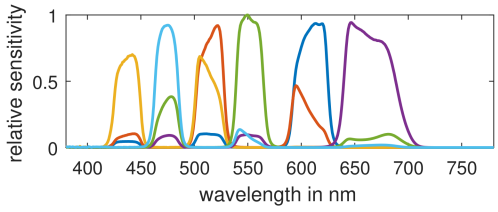

(d) 6D Stereo System

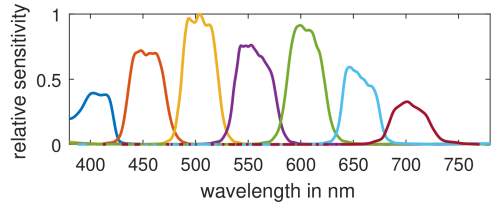

(e) 7D filter wheel camera

Figure 2: The spectral sensitivity functions of different camera systems.

2.2. Quantification of Metamer Mismatching

All possible combinations of camera systems and illuminants were considered, forming distinct color mechanisms. Each color mechanism was evaluated over the 1600 objects which are part of the Munsell glossy edition [1]. The spectral object reflectances are publicly available from the Eastern University of Finland (UEF) and were measured using a spectrophotometer in the wavelength interval 380nm to 780nm at 1nm resolution. The data set systematically covers a wide range of possible tristimulus values when viewed by the CIE standard observer under illuminant D65.

All 1600 spectral object reflectances were virtually viewed by all color mechanisms to create the corresponding color signals using Equation 1. The respective MMBs associated with a change to the CIE standard observer under the illuminant D65 were computed. All MMBs were quantified in terms of the metamer mismatch index (MMI) [12], which is defined as the Euclidean volume of the MMB in relation to the Euclidean volume of the object color-solid.

3. Results & Discussion

3.1. Sampling of the MMB-Surface

The computation of the Euclidean volume of the MMB heavily relies on the amount of computed boundary points. The finer the boundary surface is sampled, the more accurate the computed volume will become. It is therefore necessary to examine, which tessellation order is required to achieve representative results. This was achieved by computing a total of 100 different MMBs using a high tessellation order of seven, corresponding to 163.842 sampling points for each surface. All of the MMBs are associated with a change of a color mechanism consisting of different combinations of imaging systems and illuminants towards the CIE standard observer under D65. Figure 3a displays a typical example of how the computed Euclidean volume enclosed by the boundary points evolves as the tessellation order increases. It can be seen that here is a strong convergence towards its true value.

Unfortunately, it is impractical to compute all MMBs over the entire data set using a high tessellation order, since the computational cost involved becomes too high. Instead, a tessellation order of four was used throughout this work, corresponding to 2562 sampling points, which could be computed using two Intel Xeon E5-2697 processors, basically offering 48 cores at 3.5 GHz.

To assess the accuracy of a tessellation order of four, the mentioned set of the one hundred MMBs at high sampling is considered. Since volumes of different MMBs differ severely in size, they were normalized by their respective volume when using a tessellation order of seven. This allows for a better comparison. All computed volumes are showing the same trend as in Figure 3a, namely a fast convergence towards their true volume. Figure 3b displays the evolution of multiple relative volumes, including the best and worst cases that were observed. In the worst observed cased, the computed volume at a tessellation order of four was slightly above 90% of the volume achieved when using a tessellation order of seven. The best cases are beyond 99%. The mean achieved percentage is 95.1%, which is considered as acceptable.

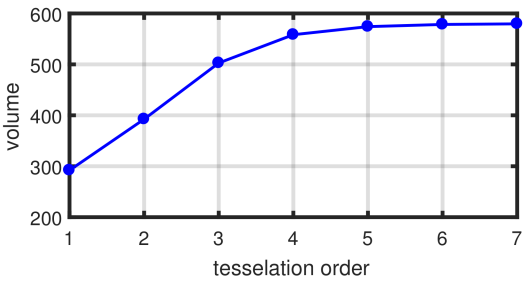

(a) Exemplary evolution of the volume for an individual MMB.

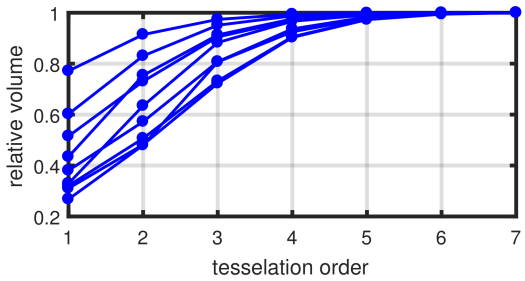

(b) Evolution of relative volumes for different MMBs.

Figure 3: The precision of computed metamer mismatch volumes is dependent on the tessellation order.

3.2. Simulated Cameras vs. Actual Cameras

Table 1 displays the result of the performed analysis for each change of color mechanism evaluated over the 1600 spectra in terms of the MMI and its respective mean value, maximum value, and standard deviation.

Based on the performed analysis, several observations can be made. First of all, when only the simulated cameras are considered, the MMI decreases with an increase in channels under all illuminants, which is in direct accordance with the results of previous studies [13, 23]. The dependency of the MMI on the amount of channels is visualized for different illuminants in Figure 4.

It can be seen from both Table 1 as well as Figure 4, that the MMI heavily relies on the illuminant under which a camera system views the object. Out of all considered illuminants, especially the illuminant F11 has the most negative impact onto the MMI. This is as well in direct accordance with previous studies [3, 20]. It should be explicitly noted, that the influence of the illuminant onto the severity of metamer mismatching also depends on the viewed object itself. Table 1 only displays the average over all spectra and while the illuminant F11 actually turns out to have the biggest MMI for every individual spectrum of the 1600 Munsell spectra, there might be spectra not being part of this data set for which this is not the case [3]. Still, this study is in accordance with the general rule of thumb,

		Sim3	Sim4	Sim5	Sim6	Sim7	Sim8	Sim9	RGB	Stereo 6	Wheel 7
E	mean	0.076	0.023	1.6e-3	2.7e-4	7.8e-5	4.2e-5	2.8e-5	6.6e-3	0.052	0.014
	max	0.247	0.084	5.0e-3	8.4e-4	2.4e-4	1.4e-4	9.4e-5	0.019	0.078	0.028
	std	0.073	0.023	1.4e3	2.5e-4	7.1e-5	4.0e-5	2.7e-5	5.6e-3	0.016	7.7e-3
D50	mean	0.052	0.017	7.4e-4	1.6e-4	3.9e-5	2.3e-5	1.4e-5	3.7e-3	0.052	0.015
	max	0.167	0.056	2.3e-3	5.0e-4	1.3e-4	7.3e-5	4.4e-5	0.010	0.080	0.029
	std	0.049	0.016	6.8e-4	1.5e-4	3.7e-4	2.1e-5	1.3e-5	3.0e-3	0.017	8.2e-3
D65	mean	0.056	0.017	7.8e-4	1.9e-4	4.5e-5	2.3e-5	1.8e-5	3.8e-3	0.049	0.015
	max	0.184	0.061	2.4e-3	6.1e-4	1.4e-4	7.4e-5	5.7e-5	0.010	0.072	0.028
	std	0.054	0.018	7.2e-4	1.9e-4	4.2e-5	2.1e-5	1.7e-5	3.1e-3	0.015	7.8e-3
D99	mean	0.062	0.017	7.3e-4	2.7e-4	4.5e-5	2.3e-5	1.8e-5	5.6e-3	0.045	0.015
	max	0.206	0.059	2.2e-3	8.6e-4	1.5e-5	7.5e-5	5.7e-5	0.019	0.066	0.028
	std	0.060	0.017	6.6e-4	1.9e-4	4.2e-5	2.1e-5	1.7e-5	4.8e-3	0.013	7.8e-3
A	mean	0.059	0.012	1.0e-3	1.5e-4	8.3e-5	3.6e-5	1.4e-5	0.015	0.065	0.019
	max	0.181	0.041	3.2e-3	4.6e-4	2.7e-4	1.2e-4	4.1e-5	0.045	0.106	0.037
	std	0.054	0.012	9.3e-4	1.3e-4	7.8e-5	3.4e-5	1.2e-5	0.013	0.023	0.010
C	mean	0.050	0.016	2.1e-3	4.0e-4	1.4e-4	8.4e-5	6.2e-5	6.4e-3	0.049	0.014
	max	0.159	0.054	6.9e-3	1.2e-3	4.4e-4	2.6e-4	2.0e-4	0.019	0.073	0.026
	std	0.047	0.016	2.0e-3	3.5e-4	1.3e-4	7.7e-5	5.8e-5	5.7e-3	0.015	7.4e-3
F4	mean	0.022	7.0e-3	5.8e-3	3.5e-3	1.7e-3	5.0e-4	6.2e-5	0.017	0.087	0.025
	max	0.057	0.020	0.017	0.010	4.7e-3	2.6e-4	8.9e-4	0.046	0.145	0.050
	std	0.017	5.9e-3	5.0e-3	3.1e-3	1.4e-3	7.7e-5	2.7e-4	0.014	0.035	0.014
F8	mean	0.050	0.017	6.5e-3	2.2e-3	5.5e-4	4.9e-4	3.2e-4	0.021	0.066	0.020
	max	0.149	0.056	0.020	6.9e-3	1.4e-3	1.5e-3	9.8e-4	0.057	0.103	0.042
	std	0.044	0.016	6.0e-3	2.0e-3	4.5e-4	4.7e-4	3.0e-4	0.017	0.022	0.012
F11	mean	0.135	0.103	0.092	0.080	0.067	0.056	0.050	0.135	0.161	0.088
	max	0.287	0.237	0.228	0.208	0.178	0.139	0.123	0.311	0.276	0.172
	std	0.085	0.070	0.066	0.060	0.050	0.040	0.036	0.092	0.070	0.048

Table 1: Computed MMIs resulting from a change of a color mechanism towards the CIE standard observer under illuminant D65 evaluated over the 1600 Munsell spectra. The standard deviation of all simulated systems displayed in this table is $\sigma = \sigma_n$.

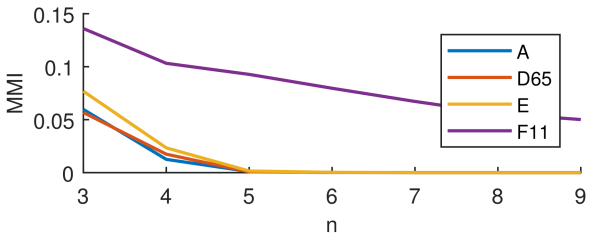

Figure 4: Evolution of the mean MMI over the channel count of the simulated camera systems with $\sigma = \sigma_n$ under different illuminants.

that when narrow band peaks appear in the SPD of an illuminant, more channels are necessary to measure color appropriately.

It has already been observed in previous studies, that the MMB varies systematically with the Munsell value and chroma [12, 27]. The conducted simulation in this work validates this result as well. Based on the given reflectance spectra, the corresponding coordinates inside the CIELAB space [2] can be computed assuming the CIE standard observer under illuminant D65. Figure 5a displays the MMI over the CIELAB coordinates encoded in the color in case of the 6D simulated system under illuminant A. It can be seen, that for different planes of constant lightness, the MMI increases towards the achromatic axis. It was already proposed, that metamer mismatching might be separated into chromaticity mismatching and luminance mismatching [12]. Figure 5b displays the MMIs of all neutral colors contained in the data set over their respective lightness value. Since the lightness is known to be a good approximation of the Munsell value, the MMI behaves over the lightness as shown in Figure 5b analogously to the MMI over the Munsell value [12]. Metamer mismatching is the most severe, when viewing the neutral objects.

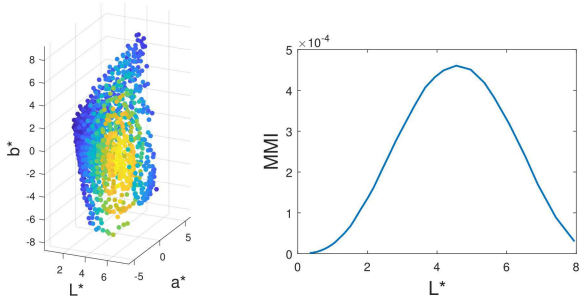

(a) The MMI for all objects (b) The MMI for all neutral objects

Figure 5: The variance of the MMI over the CIELAB space in case of the 6-channel simulated camera with $\sigma = \sigma_6$ under illuminant A.

So far, only the simulated camera systems with $\sigma = \sigma_n$ were considered, indicating that the use of multi-spectral imaging leads to a significant reduction of metamer mismatching in terms of the MMI when converting towards the human observer under D65. However, when considering the results in Table 1 achieved with the three real world imaging systems, the premise appears to be broken. It can be clearly seen that when using the real world multi-spectral imaging systems, the MMI increases drastically. Especially the fact that the RGB-camera is outperforming the multi-spectral imaging systems raises the question how the simulated and real world systems differ.
When comparing the spectral sensitivities of the simulated system shown in Figure 2a with the filter wheel camera shown in Figure 2e, it can be seen that there is a strong overlap of neighboring channels in case of the simulated system, whereas in case of the filter wheel camera, there is no such overlap. In contrast, the RGB-camera shown in Figure 2c actually has overlapping channels and it performs reasonably well (fitting in somewhere between the 4D and 5D simulated system and considering, that the simulated Gaussians are naively chosen).

3.3. Influence of the Filter Width

In order to evaluate the influence of the filter width onto metamer mismatching, it was analyzed how the simulated systems perform, when their individual channels become more narrowband. This was investigated by varying the standard deviation, σ, of the Gaussians modeling the spectral sensitivity functions. Unfortunately, the computational cost involved is too high when evaluating over the entire 1600 spectra for all possible combinations of channel count, standard deviation and illuminant, especially for the systems of higher dimensionality. Thus, the evaluation was restricted to the respective neutral spectrum from the data set as the worst case possible in terms of associated metamer mismatch volume.
Independent of the illuminant, there is always the same trend to be observed. The result corresponding to the illuminant A at the camera side is visualized in Figure 6a. The general dependency of the standard deviation, i.e. filter width, onto the MMI is directly visible. Since the individual channels of a n-dimensional camera system are distributed equidistantly in the same wavelength range from 400nm to 700nm, the central positions of neighboring channels are the closer to each other, the higher their total count is. Therefore, the simulated systems with a high channel count require a lower filter width to achieve an equivalent overlap of neighboring channels in comparison to the systems with a low channel count. In order to achieve a better comparability of systems with different channel counts, the standard deviation σ is related to the actual distance between the central positions of neighboring channels, σ_n, leading to Figure 6b.
All of the curves but the one corresponding to the 3-channel system begin to align and follow the same behavior. Decreasing the relative filter width leads to a rapid increase of the MMI, whereas increasing the relative filter width does not seem to have such a strong effect. While the filter width being too small influences all systems in a comparable way independent of the channel count, the influence of the filter width being too large is the more severe, the lower the channel count becomes. Both cases can be explained as follows. If the individual filters become too narrow band, there will be blind spots in between neighboring channels. These blind spots potentially introduce an uncertainty regarding the viewed spectral object reflectances, leading to an increase in the set of metameric reflectance spectra. Likewise, when neighboring channels begin to overlap too much, they basically yield the same information and there is no actual gain in having distinct channels.
In order to relate the results of this section to the previous real world systems, the individual channels of the 7D filter wheel camera were fitted using Gaussians. A relative standard deviation of 0.22 is roughly equivalent to the filter wheel system. It is directly visible from Figure 6b that all the simulated systems are now performing significantly worse. Especially noteworthy is Table 2, showing the MMI for all simulated systems at $\sigma = 0.2\sigma_n$ under illuminant A. All of the values are really large, when compared against the ones shown in Table 1, and there is no real decrease of MMI as the amount of channels increases.

3.4. The Importance of Smoothness

Multi-spectral imaging is generally considered as advantageous for the task of color managament. However, the results shown in this work are only partly in accordance with this assumption. While the evaluation of simulated camera

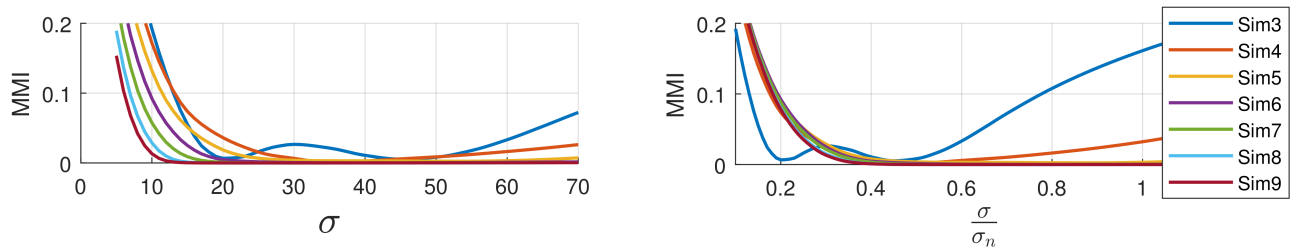

(a) MMI over standard deviation

(b) MMI over standard deviation relative to the distance of neighboring channels

Figure 6: The MMI of different simulated camera systems when viewing a gray surface under illuminant A over the filter width.

n	3	4	5	6	7	8	9
MMI	8e-3	0.08	0.10	0.11	0.10	0.09	0.09

Table 2: MMIs for the simulated camera systems with $\sigma = 0.2\sigma_n$ under illuminant A.

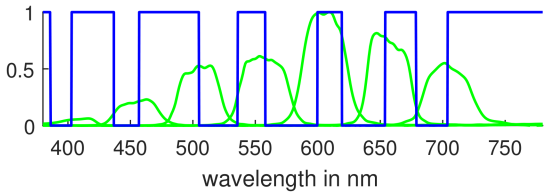

(a)

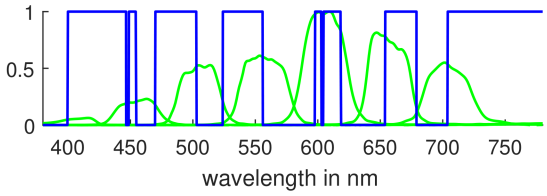

(b)

Figure 7: Two metameric reflectance functions (blue) with respect to the 7D filter wheel camera under illuminant A (green), representing boundary points of the theoretical MMB when changing towards the CIE standard observer under D65.

systems with $\sigma = \sigma_n$ showed the expected results, namely a decreasing MMI with an increasing channel count, those results could not be reproduced when using real multi-spectral imaging systems. However, the results of the real world systems could be confirmed and reproduced by changing the standard deviation of the simulated systems such that they better represent the real world systems.

The usage of multi-spectral imaging systems like the ones evaluated in this work are known to significantly increase the potential color accuracy, when used in conjunction with target-based algorithms [25], or based on spectral reconstruction techniques [10]. Thus, there must exist an important difference to the model-based algorithm used within this work.

It is due to the assumptions regarding the spectral object reflectances made by current algorithms capable of calculating the theoretical MMB [5, 12, 23]. They only assume the spectral object reflectances to be within the interval [0, 1]. The assumption itself is valid in most cases, basically neglecting gloss and fluorescence. However, there is no constraint on the smoothness of spectral object reflectances, whereas real world spectra actually are known to be smooth [6]. This might lead to more object reflectances being accounted for than appear in reality. The lack of smoothness constraints is where the difference to target based methods comes in. Since they are trained upon real world spectra, they naturally consider their characteristics, including smoothness.

Figure 7 visualizes the problem explicitly. Since there are no smoothness constraints, the boundary surface of the MMB is associated with metameric spectral reflectances consisting of a sum of elementary step functions [12]. For example, the small irruptions appearing in Figure 7b around the wavelengths 450nm and 600nm are hardly realistic. Smoothness is also of great relevance for potential blind spots between neighboring channels. If the viewed object reflectance cannot change drastically within a small wavelength step, but is subject to smoothness constraints, having blind spots is perfectly acceptable. As an example consider the flank around 540nm in Figure 7a, which moves to a wavelength around 520nm in Figure 7b.

4. Conclusion

In this work, the influence of multi-spectral imaging onto the severity of metamer mismatching was examined, when converting an observed camera signal towards the

CIE standard observer under illuminant D65. The evaluation of two multi-spectral imaging systems, a 6-channel stereo system and a 7-channel filter wheel camera, showed a drastic increase in terms of the MMI, especially in comparison to an evaluated RGB-camera. Since the MMI represents the relative metamer mismatch volume, this corresponds to the multi-spectral imaging systems having a higher uncertainty about the potential object appearance, when viewed by a human observer, than the evaluated RGB-camera. This effect was attributed to a lack in assumptions made by current algorithms capable of computing the theoretical boundary of the MMB, neglecting the smoothness of spectral object reflectances.

The essence of this work is that current algorithms capable of calculating the precise theoretical MMB, while certainly being impressive and showing promising results, are lacking a very important constraint in form of the smoothness of spectral object reflectances. This should always be kept in mind, when considering their results, since it leads to the calculated MMBs being larger than it can be expected in reality.

References

[1] *Munsell Book of Color - Glossy Finish Collection*. (Munsell Color, Baltimore, Md., 1976).

[2] Colorimetry, Volume 15.3 of CIE publications. Technical report, 2004.

[3] R. S. Berns, M. D. Fairchild, and M. M. Beering. Quantification of illuminant metamerism for four coloration systems via metameric mismatch gamuts. *Color Research & Application*, 13(6):346–357, 1988.

[4] P. Centore. A zonohedral approach to optimal colours. *Color Research & Application*, 38(2):110–119, 2013.

[5] P. Centore. An open-source algorithm for metamer mismatch bodies. Technical report, 2017.

[6] M. Flinkman, H. Laamanen, P. Vahimaa, and M. Hauta-Kasari. Number of colors generated by smooth nonfluorescent reflectance spectra. *J. Opt. Soc. Am. A*, 29(12):2566–2575, Dec 2012.

[7] M. R. L. Guowei Hong and P. A. Rhodes. A study of digital camera colorimetric characterization based on polynomial modeling. *Color Research & Application*, 26(1):76–84, 2001.

[8] V. Heikkinen, R. Lenz, T. Jetsu, J. Parkkinen, M. Hauta-Kasari, and T. Jääskeläinen. Evaluation and unification of some methods for estimating reflectance spectra from rgb images. *J. Opt. Soc. Am. A*, 25(10):2444–2458, Oct 2008.

[9] H. E. Ives. *The transformation of color-mixture equations from one system to another*. J. Franklin Inst., 1915.

[10] J. Klein and T. Aach. Number of colors generated by smooth nonfluorescent reflectance spectra. *Conference on Colour in Graphics, Imaging, and Vision*, (8):239–146, 2012.

[11] Z. Liu, Q. Liu, G. ai Gao, and C. Li. Optimized spectral reconstruction based on adaptive training set selection. *Opt. Express*, 25(11):12435–12445, May 2017.

[12] A. D. Logvinenko, B. Funt, and C. Godau. Metamer mismatching. *Trans. Img. Proc.*, 23(1):34–43, Jan. 2014.

[13] A. D. Logvinenko, B. Funt, and C. Godau. How metamer mismatching decreases as the number of colour mechanisms increases with implications for colour and lightness constancy. *Vision Research*, 113:65–70, 2015.

[14] R. Luther. Aus dem Gebiet der Farbreizmetrik. *Zeitschrift für technische Physik*, 8:540–558, 1927.

[15] L. T. Maloney. Evaluation of linear models of surface spectral reflectance with small numbers of parameters. *J. Opt. Soc. Am. A*, 3(10):1673–1683, Oct 1986.

[16] A. Mansouri, F. Marzani, and P. Gouto. Neural networks in cascade schemes for spectral reflectance reconstruction. In *IEEE International Conference on Image Processing*, pages 718–721, Genova, Italy, 2005.

[17] F. Martinez-Verdu, J. Puyol, and P. Capilla. Characterization of a digital camera as an absolute tristimulus colorimeter. *Journal of Imaging Science and Technology*, 47(4):279–295, 2003.

[18] J. L. Nieves, E. M. Valero, S. M. C. Nascimento, J. Hernández-Andrés, and J. Romero. Multispectral synthesis of daylight using a commercial digital ccd camera. *Appl. Opt.*, 44(27):5696–5703, Sep 2005.

[19] D. Paulus, J. Hornegger, and L. Csink. Linear approximation of sensitivity curve calibration. In *8. Workshop Farbbildverarbeitung*, pages 3–10, Illmenau, Germany, 2002.

[20] S. Peyvandi, S. H. Amirshahi, and B. Sluban. Illuminant metamerism potentiality of metameric pairs. *Coloration Technology*, 128(5):341–349, 2012.

[21] W. K. Pratt and C. E. Mancill. Spectral estimation techniques for the spectral calibration of a color image scanner. *Appl. Opt.*, 15(1):73–75, Jan 1976.

[22] M. Shi and G. Healey. Using reflectance models for color scanner calibration. *J. Opt. Soc. Am. A*, 19(4):645–656, Sep 2002.

[23] T. Stiebel, B. Hill, and D. Merhof. On the theory of metamer mismatching. Technical report, 2017.

[24] G. Wyszecki and W. S. Stiles. *Color Science: Concepts and Methods, Quantitative Data and Formulae*. John Wiley & Sons, 2 edition, 2000.

[25] M. Yamaguchi, M. Mitsui, Y. Murakami, H. Fukuda, N. Ohyama, and Y. Kubota. Multispectral color imaging for dermatology: Application in inflammatory and immunologic diseases. In *13th Color and Imaging Conference*, pages 52–58, 2005.

[26] Z. Yan, H. Zhang, B. Wang, S. Paris, and Y. Yu. Automatic photo adjustment using deep neural networks. *ACM Trans. Graph.*, 35(2):11:1–11:15, 2016.

[27] X. Zhang, B. Funt, and H. Mirzaei. Metamer mismatching in practice versus theory. *J. Opt. Soc. Am. A*, 33(3):A238–A247, 2016.

[28] Y. Zhao and R. S. Berns. Image-based spectral reflectance reconstruction using the matrix r method. *Color Research & Application*, 32(5):343–351, 2007.